

Chandra HETG X-ray Spectra and Variability of π Aqr, a γ Cas-type Be star.

DAVID P. HUENEMOERDER,^{1,*} PRAGATI PRADHAN,² CLAUDE R. CANIZARES,¹ SEAN GUNDERSON,¹ RICHARD IGNACE,³
JOY S. NICHOLS,⁴ A. M. T. POLLOCK,⁵ NORBERT S. SCHULZ,¹ DUSTIN K. SWARM,⁶ AND JOSÉ M. TORREJÓN⁷

¹ Kavli Institute for Astrophysics and Space Research, Massachusetts Institute of Technology, 77 Massachusetts Ave., Cambridge, MA 02139, USA

² Embry Riddle Aeronautical University, Department of Physics & Astronomy, 3700 Willow Creek Road Prescott, AZ 86301, USA

³ Department of Physics & Astronomy, East Tennessee State University, Johnson City, TN 37614 USA

⁴ Harvard & Smithsonian Center for Astrophysics, 60 Garden St., Cambridge, MA 02138, USA

⁵ Department of Physics and Astronomy, University of Sheffield, Hounsfield Road, Sheffield S3 7RH, UK

⁶ Department of Physics and Astronomy, University of Iowa, Iowa City, IA, USA

⁷ Instituto Universitario de Física Aplicada a las Ciencias y las Tecnologías, Universidad de Alicante, E- 03690 Alicante, Spain

ABSTRACT

High-resolution X-ray spectra of π Aqr, a γ Cas-type star, obtained with the *Chandra*/HETG grating spectrometer, revealed emission lines of H-like ions of Mg, Si, S, and Fe, a strong, hard continuum, and a lack of He-like ions, indicating the presence of very hot thermal plasma. The X-ray light curve showed significant fluctuations, with coherent variability at period of about 3400 s in one observation. The hardness ratio was relatively constant except for one observation in which the spectrum was much harder and more absorbed. We interpret the X-ray emission as arising from accretion onto the secondary, which is likely a magnetic white dwarf, an intermediate polar system.

Keywords: Be stars (142), White dwarf stars (1799), X-ray astronomy (1810), High resolution spectroscopy (2096), Gamma Cassiopeiae stars (635), Early-type emission stars (428)

1. INTRODUCTION

π Aqr was recently identified as a γ Cas-type star by Nazé et al. (2017). The γ Cas-types are O/Be stars which in X-rays have unusually hard spectra, with characteristic temperatures exceeding 100 MK (8.6 keV), yet appear to be thermal due to presence of Fe XXV and Fe XXVI emission lines. Given their thermal spectrum and low X-ray luminosities, their nature as accreting X-ray binaries containing a neutron star or a black hole companion is ruled out. Several γ Cas types are known to be some form of binary including π Aqr (Bjorkman et al. 2002): it is the nature of the companion which makes them of special interest. Postnov et al. (2017) proposed a neutron star where direct accretion is impeded magneto-centrifugally, the so called propeller state. Langer et al. (2020) gave an account of possible evolutionary states, with preference for stripped-core companions, either SdO or He-stars. Gies et al. (2023) argued that SdO companions would be bright enough to see optically, so they prefer a white dwarf companion hypothesis. Tsujimoto et al. (2018), based on X-ray spectral modeling of two γ Cas-type stars, also prefer a white dwarf companion. In *XMM-Newton* spectra of π Aqr, Nazé et al. (2017) found a

plasma temperature of about 10 keV (116 MK) from isothermal fits of thermal spectra, and found no significant emission line features in the lower-energy RGS spectral band. In *Swift* data, Nazé et al. (2019) had similar results requiring an isothermal plasma with $kT = 15$ keV ($T = 174$ MK), and local absorption of about $N_{\text{H}} = 0.5 \times 10^{22} \text{ cm}^{-2}$. Tsujimoto et al. (2023) modeled *NuSTAR* and *XMM-Newton* spectra of π Aqr and found a maximum temperature of 19 keV (220 MK) from a cooling flow model (Pandel et al. 2005), concluding that π Aqr could host either a magnetic or non-magnetic white dwarf. The interferometric survey of Be stars by Klement et al. (2024) included several γ Cas-type stars with X-ray emission. They failed to detect any companions, and excluded SdO and main-sequence companions for π Aqr, leaving a white dwarf as the most viable secondary and source of X-ray emission.

Here we present X-ray spectral and temporal properties of π Aqr revealed by recent *Chandra*/HETG observations. § 2 details the observations and reduction of the *Chandra* HETG data. The spectra are described and interpreted through spectral modeling in § 3. Finally in § 4 we comment on variability observed in our dataset, in particular a notable hardening of the spectra arising from a jump in absorbing column density during the last of our observational sets.

* dph@mit.edu

Table 1. π Aqr Observational Information

ObsID	DATE-OBS	Exposure	ϕ_{orb}
	[<i>Chandra</i> start date]	[ks]	
26079	2022-08-23T15:37:02	9.93	0.40
27269	2022-08-27T04:24:31	9.99	0.44
26080	2022-09-05T00:58:47	29.67	0.54
26001	2022-09-13T00:14:35	19.80	0.64
27412	2022-09-14T06:16:23	21.78	0.65
27325	2022-10-30T09:44:35	9.76	0.20

NOTE—The orbital phase is defined as 0.0 for the maximum radial velocity (redshift) of the secondary, using the error-weighted-mean ephemeris of Bjorkman et al. (2002): $T_0 = 2450274.84$ JD, $P = 84.132$ day.

2. OBSERVATIONS AND PROCESSING

We obtained *Chandra*/HETG data for π Aqr in six observations made during August to October, 2022, for a total exposure of 101 ks. Details are provided in Table 1.¹ Canizares et al. (2005) gave a description of the instrument. Data were processed with CIAO (Fruscione et al. 2006) following standard procedures, except for use of a narrower spatial region defining the HEG and MEG loci. This removes ambiguity between the two grating types at the shortest wavelengths, and can improve flux determination below ~ 1.8 Å in particular for hard sources where standard regions overlap. Spectra were analyzed using the ISIS package (Houck & Denicola 2000) in conjunction with AtomDB (Foster et al. 2012). For timing analysis, we used the SITAR ISIS package², as distributed with ISISscripts.³

3. SPECTRUM AND MODELING

We analyzed the spectrum in two parts because one observation, with about 10 ks of the 100 ks total exposure, had a very different character in terms of hardness (see § 4 for variability details). We show the low hardness ratio state HETG spectrum in the left side of Figure 1, where strong Fe XXV (1.85 Å) and Fe XXVI (1.78 Å) emission lines are seen, with a shoulder on the red side of the He-like line that may be Fe K α fluorescence. The rest of the spectrum clearly shows

the H-Ly α -like emission lines from S XVI (4.73 Å), Si XIV (6.18 Å), and Mg XII (8.42 Å) on top of a strong continuum. There may be some Fe XXIV emission lines near Mg XII and between 10–13 Å. The He-Ly α -like emission lines from S, Si, and Mg are conspicuous in their absence. These characteristics point to very high-temperature plasmas; the H-like lines, except for Fe, are weak because the plasma is dominated by temperatures well above the peaks of the emissivity functions, on the long tail of the H-like emissivities and well beyond the significant region of He-like emissivity. In an isothermal plasma, to obtain a limit in the Si XIII to Si XIV flux less than the observed ratio of < 0.10 requires a temperature greater than 42 MK, and to obtain the observed ratio of Fe XXVI to Fe XXV requires a temperature of at least 70 MK.

To characterize the spectrum more systematically, we have fit a few-temperature model using AtomDB emissivities. For such a hot plasma, the continuum shape provides limited leverage on the temperature, since above about 100 MK, the turnover of the thermal bremsstrahlung occurs below 2 Å, and the shape above that is largely flat and featureless. We find that three temperatures are sufficient to describe the spectrum, to which we added a Gaussian for the possible Fe K α fluorescence. Each temperature component shared a common Doppler shift and “turbulent” broadening term for any Gaussian intrinsic width. Instrumental broadening is handled by forward-folding through the calibrated responses, and common elemental abundances, for which Mg, Si, S, and Fe were free to vary. However, for few-temperature plasmas, abundances are degenerate with temperature since there are two ways to change a model line flux: vary the temperature, or vary the abundance. Should the temperature not be accurate, the abundance will be not be accurate as well. We also include a single absorption term, however note that the foreground interstellar absorption is small in this band ($\sim 0.03 \times 10^{22} \text{ cm}^{-2}$, Gudennavar et al. (2012)).

The fit converges on a very hot component to produce enough Fe XXVI and to provide the correct shape between 1.7 Å and 3 Å. However, the Fe XXVI flux is rather uncertain by about 40%, so anything over ~ 200 MK would be adequate. A component of about 40 MK is required to give the observed Fe XXV flux, some Fe XXVI, and most of the S XVI emission, plus Si XIV, Mg XII, and Fe XXIV. The third component, at 10 MK also contributes to the H-like series, and to the Fe XXIV ionization, but this component has the lowest normalization. However, if larger, it would contribute to Si XIII, which is weak or absent. The emission measure, for a distance of 286 pc (Gaia Collaboration et al. 2016, 2018) is $1.0 \times 10^{55} \text{ cm}^{-3}$. The absorption required is $N_{\text{H}} \sim 0.4 \times 10^{22}$, which has a transmission factor of about 0.3 at 13 Å. The absorbed model flux in the 0.5–10 keV band is $1.5 \times 10^{-11} \text{ erg cm}^{-2} \text{ s}^{-1}$, and the X-ray luminosity is $1.8 \times 10^{32} \text{ erg s}^{-1}$. The lines required some

¹ Data are available at <https://doi.org/10.25574/ObsID>, where *ObsID* is to be replaced with the values from Table 1.

² For a description of SITAR routines, see <https://space.mit.edu/cxc/analysis/SITAR/>.

³ The ISISscripts package is available from <http://www.sternwarte.uni-erlangen.de/isis/>.

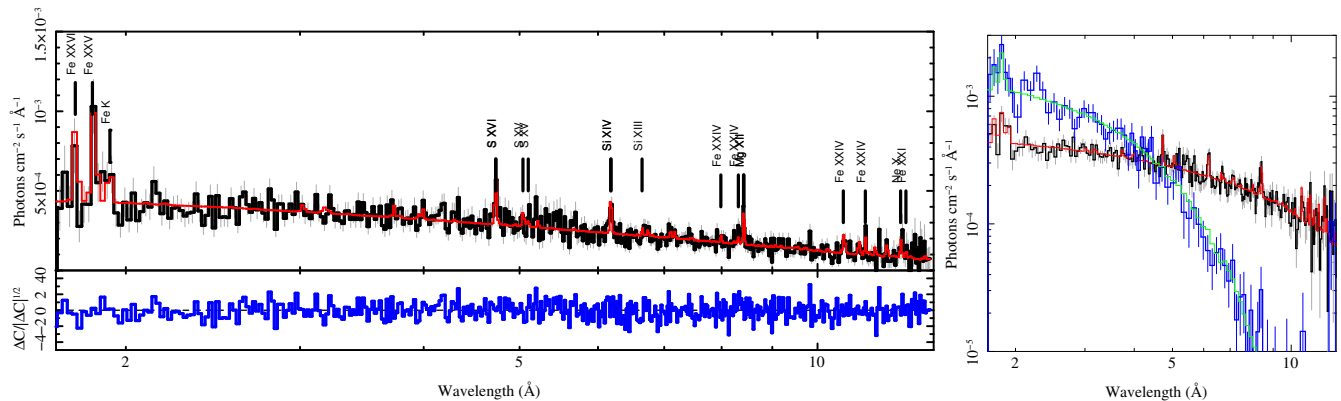


Figure 1. Left: HETG spectrum of π Aqr in black, which is the merged HEG and MEG first orders, excluding the high hardness ratio observation (27325). In red is a model using three APEC components plus a Gaussian for the putative Fe K fluorescence. On the right, we compare the high hardness ratio state spectrum (blue) to the rest (black and red).

broadening beyond instrumental, with a turbulent velocity term of $\sim 400 \text{ km s}^{-1}$, which corresponds to S XVI, Si XIV and Mg XII full-widths, half-maxima ($FWHM$ s) of about 900 km s^{-1} (for $T = 40 \text{ MK}$). The Doppler shift from the global fit was $+64 \pm 66 \text{ km s}^{-1}$, without correction for the line-of-sight velocities at these epochs, which is less than 7 km s^{-1} . The range is incommensurate with the Bjorkman et al. (2002) solution for the secondary at these phases of about -70 km s^{-1} . Plasma model details are given in Table 2.

We have also fit the few emission lines with intrinsic Gaussian profiles, folded through the instrument response, in order to determine fluxes, velocity offsets, and widths. The features with signal-to-noise ratio > 3 and which have good resolution are Si XIV and Mg XII. These have $FWHM \sim 800 \text{ km s}^{-1}$, consistent with the plasma model determination. Their Doppler shifts are consistent with 0 km s^{-1} . Line fit details are given in Table 3.

The right panel of Figure 1 shows the high hardness state spectrum compared to the low hardness state. We see that the high hardness state is brighter below 4 Å, but much more absorbed. We fit this hard state spectrum with a two temperature model since less information is available from emission lines - only Fe XXV, being so heavily absorbed, and having only 10 ks exposure. The plasma is much hotter, has higher flux, and much greater absorption. Details are given in Table 2

Table 2. π Aqr Plasma Model Fit Parameters

Parameter	Value	σ	Value	σ	Unit
	Normal HR		High HR		
T_1	270	94	> 520		MK
T_2	44	11	70	20	"
T_3	13	3			"
$norm_1$	7.3	0.8	21.1	3.6	10^{-11} cm^{-5}
$norm_2$	2.7	1.0	6.0	2.8	"
$norm_3$	0.4	0.3			"
v_{turb}	404	169			km s^{-1}
Δv	64	66			"
$A(\text{Mg})$	1.2	0.3			Relative to Solar
$A(\text{Si})$	0.7	0.2			"
$A(\text{S})$	1.3	0.4			"
$A(\text{Fe})$	0.6	0.1			"
N_{H}	0.40	0.05	4.7	0.2	10^{22} cm^{-2}
EM	1.0	0.1	2.6	0.4	10^{55} cm^{-3}
f_{x}	1.50		2.54		$10^{-11} \text{ erg cm}^{-2} \text{ s}^{-1}$
L_{x}	1.81		4.38		$10^{32} \text{ erg s}^{-1}$

NOTE—“Normal HR” refers to all observations except 27325, and “High HR” is for 27325 in the high hardness-ratio state. Flux is integrated from the model over the 0.5–10 keV band. The emission measure used a distance of $D = 286$ pc, and is related to the normalizations by a factor of $10^{11} 4\pi D^2$. Relative abundances are referenced to [Anders & Grevesse \(1989\)](#). Uncertainties are 1σ .

4. VARIABILITY

It is well known that γ Cas-type stars are variable in optical and X-ray bands (Nazé et al. 2020b,c,a). Optical variability can be highly periodic and is generally attributed to the B-star’s rotation or pulsations. X-ray fluctuations can exceed factors of two or three in short times, behavior often referred to as “flaring” (but not like coronal flares in the Sun and late-

type stars, which have increases in both flux and temperature and are strongly tied to stellar magnetism).

We extracted X-ray light curves of π Aqr from the dispersed first-order events and found significant variability with about a factor of two amplitude in count rate. For the longest observation (~ 30 ks; Observation ID 26080) of the six segments, we also found significant cyclic variability,

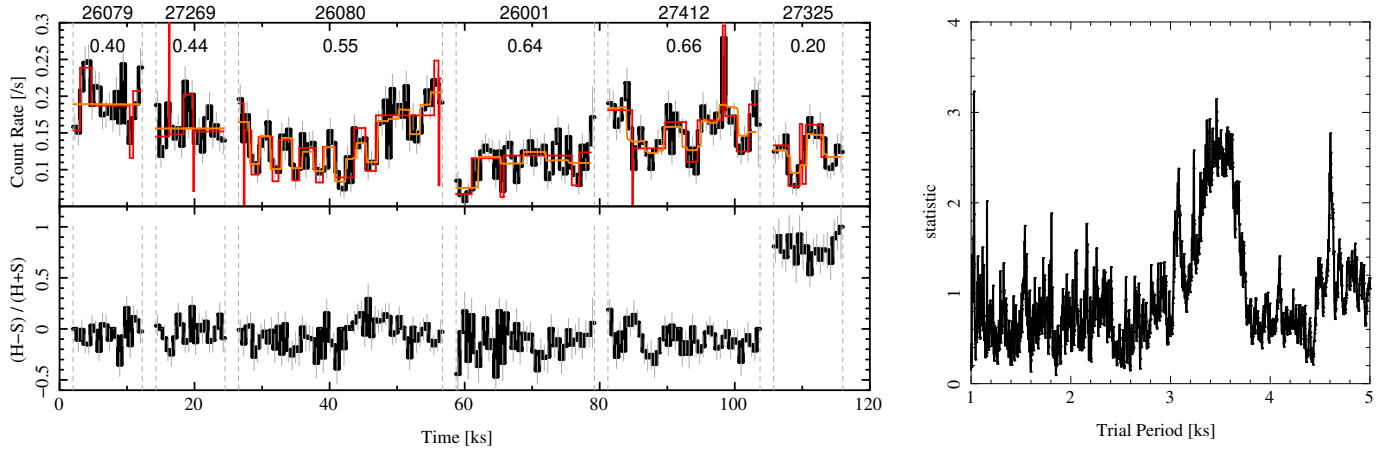


Figure 2. Left top: The X-ray light curve of π Aqr for all observations for the 1.7–13 Å band, concatenated in time order. The vertical dashed lines mark arbitrary length gaps between observations. The black curve shows the count rate in dispersed first-order events. The red and orange curves show the results of Bayesian blocks (Scargle et al. 2006; Scargle et al. 2013) and Gregory-Loredo (Gregory & Loredo 1992) algorithms, confirming the statistically significant variability. Left bottom: the count-rate hardness ratio, $(H - S)/(H + S)$, where H is the “hard” rate in the 1.7–5.2 Å band, and S in 5.2–13 Å for “soft”. The last observation (27325) does not stand out in the total rate curve, but does in hardness. Labels at the top give the observation IDs with orbital phases below them. Right: epoch folding algorithm (Davies 1990) “ L ”-statistic for obsid 26080 showing coherent variability with period near 3400 s.

Table 3. π Aqr Line Fit Parameters

Line	λ_0	Δv	σ	$10^6 \times \text{Flux}$	σ	$FWHM$	σ
	[Å]	[km s $^{-1}$]		[phot cm $^{-2}$ s $^{-1}$]		[km s $^{-1}$]	
Fe XXVI	1.7798	8.5	3.4	0.0	1320
Fe XXV	1.8554	−48	276	20.7	4.8	2372	1101
FeK α	1.94	−950	773	4.5	2.4
S XVI	4.7301	−240	630	5.3	2.1
Si XIV	6.1831	92	123	6.0	1.5	778	582
Si XIII(r)	6.6479	< 1.2
Mg XII	8.4219	28	71	9.9	1.7	840	280

NOTE—Wavelengths for Fe XXVI and Fe XXV are weighted means over the components in each group; each was fit with a single Gaussian model. The Fe XXVI offset from Fe XXV was frozen. The width of FeK α was tied to that of Fe XXVI. The S XVI width was tied to that of Si XIV, since the former has a fairly low signal-to-noise ratio. The flux limit on the Si XIII resonance line was computed with a frozen position and a width frozen at the value for Si XIV. Uncertainties are for 68% confidence intervals.

with a period of about 3400 s. In Figure 2 we show light curve and hardness ratio for all observations, and the epoch-folding period search for the segment showing the strongest periodic signal. To our knowledge, this is only the second case of a clear X-ray modulation with an approximately one hour period in a γ Cas-type star, the first being found by Lopes de Oliveira et al. (2006) in HD 161103. The other segments, which range from 10 to 22 ks exposures, had statistically significant variability, but not as strong an indication of coherence.

The hardness ratio, defined as $(H - S)/(H + S)$, with H and S defined as count rates in bands chosen to on average have equal counts (H : 1.7–5.2 Å, S : 5.2–13 Å), was relatively constant for most of the time, as we show in the left hand side of Figure 2, bottom panel. The last observation, however, stands out as extremely hard, which led us to analyze the spectrum of that state separately.

5. INTERPRETATIONS

The HETG observations presented here strongly support the case that the π Aqr B-star’s companion is an accreting white dwarf. The emission lines of H-like ions show that there is thermally emitting plasma, and that the temperature is high, given the lack of He-like ions for anything but Fe. Furthermore, the continuum is consistent with Bremsstrahlung for the same temperature required for the emission lines. Even though the spectral turnover is below 2 Å, there is some leverage in the spectral curvature in the observed band. The temperatures we have derived are consistent with free-fall accretion onto a white dwarf with mass between 0.5–0.8 M_\odot (Mukai 2017; Tsujimoto et al. 2023). This is consistent with prior *XMM-Newton* and *NuSTAR* observations, but since emission lines are weak, the HETG band and spectral resolving power were required to detect and characterize them. The best characterized lines, those of Mg XII and Si XIV, have similar widths and centroid offsets as in early B-star stellar winds, but they are an order of magnitude more luminous in π Aqr, and cooler species are missing (Pradhan et al. 2023). Consequently, the spectrum is incompatible with a superposition of a powerlaw continuum with a B-star thermal spectrum.

The detection of variability with a period of about 3400 s suggests that if the companion is a white dwarf, that it is magnetic, such as in an intermediate polar where accretion is funneled onto the white dwarf by a moderately strong global magnetic field. The period would then be rotational modulation. The breadth of the peak obtained through epoch folding is also reminiscent of the compact object being a white dwarf (see Figure 2 in Hui et al. 2012) as opposed to a neutron star where narrower peaks are expected because of the very coherent pulsations. The coherent variability was only seen in one observation, however. The others show both similar amplitude but more sporadic fluctuations and also changes in the mean flux level. One would expect under the hypothesis of an accreting white dwarf, that if the accretion is steady, and the polar region of a white dwarf always visible, then the rotational “clock’s” pulsations would be persistent. The variations are obviously due to something more complicated than a coherent rotationally modulated accretion spot. We have evidence that very large changes can occur. In addition to periodic modulation and irregular variations, there was the state with the high hardness ratio. The absorption increased by an order of magnitude, while the flux nearly doubled, and the luminosity more than doubled. We do not know if this is a random episodic or a phase-dependent event. It occurred near orbital phase 0.2, when viewing the companion behind the B-star, through the B-star wind, and perhaps downstream along the accretion column (see Tab. 1 and Fig. 2). The *Swift* monitoring by Nazé et al. (2019) also has their highest absorption near this phase.

There is precedent for complex structure in intermediate polar accretion disks, with bulges, streams, and veiling which can perturb light curves, such as has been seen in optical, UV, and X-ray observations of EX Hya (Belle et al. 2002, 2005). Hiding spin modulation in X-rays with disk instabilities is very speculative, however, and will require longer term X-ray monitoring to separate coherent modulation from other variability. One would have to either hide the accretion hot spot with strong absorption, or mask the rotational pulsations with other fluctuations. Empirically, we can say that there is sometimes coherent X-ray modulation, but also more random fluctuations, and large, persistent changes in spectral hardness. These all suggest complex and variable X-ray emitting and absorbing structures.

While our evidence is circumstantial, we suggest that the π Aqr variations indicate that a white dwarf companion is likely, given the episode of periodic variation. But there is some other source of variability which can change emission and absorption levels. We cannot determine from our dataset whether this is stochastic, episodic, or orbitally phase dependent.

EX Hya is a well studied intermediate polar with a white dwarf rotation period of about 4000 s (Warner 1983; Luna

et al. 2015), similar to our detected period in π Aqr. To compare X-ray spectra, we took our three-temperature model, removed the absorption and renormalized to the HETG-observed flux of EX Hya. We found overall qualitative agreement, but with some interesting differences. Figure 3 shows our unabsorbed model against the observed EX Hya spectrum, which has little neutral absorption ($N_{\text{H}} < 10^{20} \text{ cm}^{-2}$; Luna et al. (2015)). EX Hya has emission from the H- and He-like ions of O, Ne, Mg, Si, S, Ar, Ca, and Fe (see details in Luna et al. 2015). In π Aqr, we only see the H-like lines of Mg, Si, S, and Fe, as well as He-like Fe; longward of 13 Å, π Aqr absorption is too strong for detection at our exposure. The differences seen, however, show that the π Aqr plasma is substantially hotter than that of EX Hya, since the He-like lines are extremely weak in π Aqr. Our emission measure distribution for π Aqr, though with only 3 points, rises steadily from $\log T \approx 7.1$ to 8.5. This parallels (at about 10 times the amplitude) the simple cooling flow model of Luna et al. (2015) for EX Hya, which they rejected in favor of their empirical model which declines steeply above about 7.8 dex. Below $\log T \sim 7.1$, if we extrapolate our emission measure to follow the simple cooling flow model, we cannot tell if such plasma exists in π Aqr because the predicted fluxes are below our sensitivity limit; the hot plasma greatly overwhelms any cooler plasma signature. It could be that the putative white dwarf in π Aqr is more massive than that in EX Hya. According to Yuasa et al. (2010), a change of a few tenths of a Solar mass of a white dwarf can change the shock temperature by a factor of two. Hence, we tentatively conclude that there is a white dwarf companion in π Aqr with somewhat more mass than the one in EX Hya, which is estimated by Luna et al. (2015) to be $0.79 M_{\odot}$. The emission measure distribution of π Aqr seems consistent with a cooling flow model, but higher signal-to-noise X-ray spectra will be required to quantify the contribution of cooler plasma through detection of He-like ion emission.

Our characterization with a few-temperature, slab-absorbed model is very rudimentary. We are beginning to apply cooling flow models, in which a continuous emission measure distribution is weighted inversely by the cooling time (Mushotzky & Szymkowiak 1988; Pandel et al. 2005; Böhringer & Werner 2010). Other refinements were implemented by Tsujimoto et al. (2023), such as partial covering, and reflection models to explain Fe K fluorescence. The cooling flow models specify a mass accretion rate through the X-ray luminosity and temperature extrema. For a simple, slab-absorbed, geometry-independent (optically thin) cooling-flow model, we obtained mass accretion rates for the low and high hardness states of 4×10^{-11} and $7 \times 10^{-11} M_{\odot} \text{ yr}^{-1}$. These values are within an order of magnitude for low-accretion-rate intermediate polars. For the expected accretion disc densities at the white dwarf

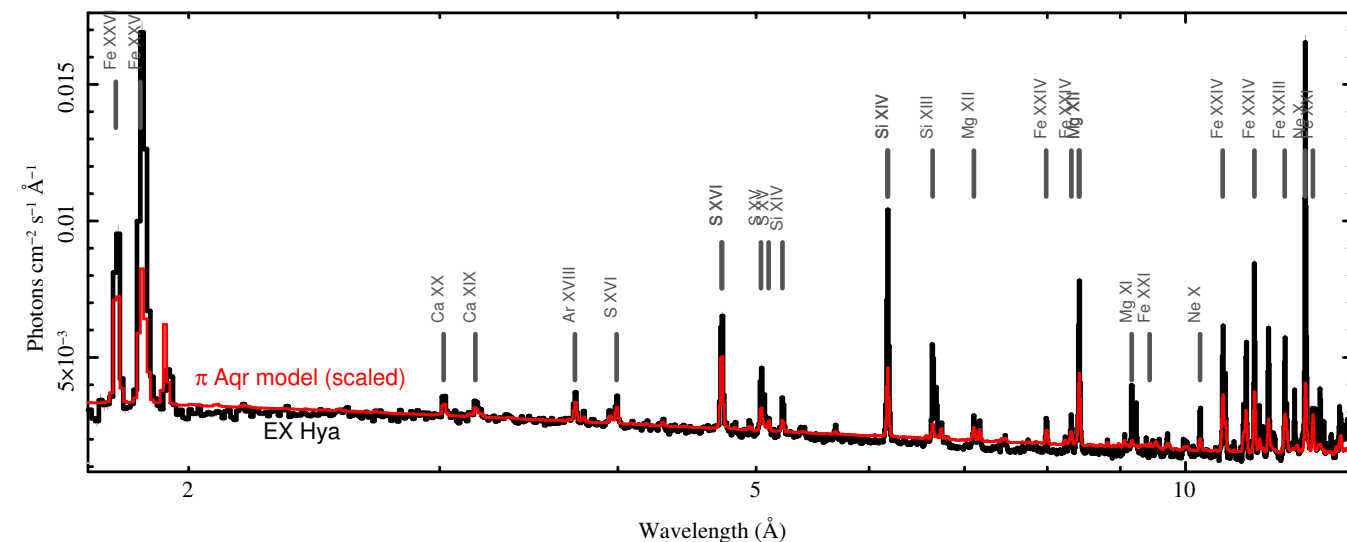


Figure 3. The π Aqr model (red), with absorption removed and renormalized to the observed mean flux of EX Hya, an intermediate polar (black). The continuum shapes are similar, but the π Aqr emission lines are weaker relative to the continuum, and especially the He-like features, which have a much lower He- to H-like ratios.

orbital separation (Jones et al. 2008), accretion rates up-to $10^{-8} - 10^{-7} M_{\odot} \text{ yr}^{-1}$ can be supported (assuming spherical accretion).

The high-resolution X-ray spectra presented here have further supported the cases put forward by [Tsujiimoto et al. \(2023\)](#) and [Klement et al. \(2024\)](#) that the dominant X-ray source in π Aqr is a magnetic white dwarf, probably an intermediate polar. Further observations are warranted, in particular long observations to monitor coherent variability, and phase-resolved coverage to separate geometric from stochastic variability.

Support for this work was provided by NASA through the Smithsonian Astrophysical Observatory (SAO) contract SV3-73016 to MIT for Support of the Chandra X-Ray Center (CXC) and Science Instruments. CXC is operated by SAO for and on behalf of NASA under contract NAS8-03060. This research has made use of ISIS functions (ISISscripts) provided by ECAP/Remeis observatory and MIT (<http://www.sternwarte.uni-erlangen.de/isis/>).

Facility: CXO (HETG/ACIS)

Software: CIAO (Fruscione et al. 2006), ISIS (Houck & Denicola 2000)

REFERENCES

- Anders, E., & Grevesse, N. 1989, *GeoCoA*, 53, 197
- Belle, K. E., Howell, S. B., Mukai, K., et al. 2005, *AJ*, 129, 1985
- Belle, K. E., Howell, S. B., Sirk, M. M., & Huber, M. E. 2002, *ApJ*, 577, 359
- Bjorkman, K. S., Miroshnichenko, A. S., McDavid, D., & Pogrosheva, T. M. 2002, *ApJ*, 573, 812
- Böhringer, H., & Werner, N. 2010, *A&A Rv*, 18, 127
- Canizares, C. R., Davis, J. E., Dewey, D., et al. 2005, *PASP*, 117, 1144
- Davies, S. R. 1990, *MNRAS*, 244, 93
- Foster, A. R., Ji, L., Smith, R. K., & Brickhouse, N. S. 2012, *ApJ*, 756, 128
- Fruscione, A., McDowell, J. C., Allen, G. E., et al. 2006, in Presented at the Society of Photo-Optical Instrumentation Engineers (SPIE) Conference, Vol. 6270, SPIE Conference Series
- Gaia Collaboration, Prusti, T., de Bruijne, J. H. J., et al. 2016, *A&A*, 595, A1
- Gaia Collaboration, Brown, A. G. A., Vallenari, A., et al. 2018, *A&A*, 616, A1
- Gies, D. R., Wang, L., & Klement, R. 2023, *ApJL*, 942, L6
- Gregory, P. C., & Lored, T. J. 1992, *ApJ*, 398, 146
- Gudennavar, S. B., Bubbly, S. G., Preethi, K., & Murthy, J. 2012, *ApJS*, 199, 8
- Houck, J. C., & Denicola, L. A. 2000, in *Astronomical Society of the Pacific Conference Series*, Vol. 216, *Astronomical Data Analysis Software and Systems IX*, ed. N. Manset, C. Veillet, & D. Crabtree, 591
- Hui, C. Y., Seo, K. A., Hu, C. P., Lin, L. C. C., & Chou, Y. 2012, *ApJ*, 759, 109
- Jones, C. E., Sigut, T. A. A., & Porter, J. M. 2008, *MNRAS*, 386, 1922
- Klement, R., Rivinius, T., Gies, D. R., et al. 2024, *ApJ*, 962, 70
- Langer, N., Baade, D., Bodensteiner, J., et al. 2020, *A&A*, 633, A40
- Lopes de Oliveira, R., Motch, C., Haberl, F., Negueruela, I., & Janot-Pacheco, E. 2006, *A&A*, 454, 265
- Luna, G. J. M., Raymond, J. C., Brickhouse, N. S., Mauche, C. W., & Suleimanov, V. 2015, *A&A*, 578, A15
- Mukai, K. 2017, *PASP*, 129, 062001
- Mushotzky, R. F., & Szymkowiak, A. E. 1988, in *NATO Advanced Study Institute (ASI) Series C*, Vol. 229, *Cooling Flows in Clusters and Galaxies*, ed. A. C. Fabian, 53
- Nazé, Y., Motch, C., Rauw, G., et al. 2020a, *MNRAS*, 493, 2511
- Nazé, Y., Pigulski, A., Rauw, G., & Smith, M. A. 2020b, *MNRAS*, 494, 958
- Nazé, Y., Rauw, G., & Cazorla, C. 2017, *A&A*, 602, L5
- Nazé, Y., Rauw, G., & Pigulski, A. 2020c, *MNRAS*, 498, 3171
- Nazé, Y., Rauw, G., & Smith, M. 2019, *A&A*, 632, A23
- Pandel, D., Córdova, F. A., Mason, K. O., & Priedhorsky, W. C. 2005, *ApJ*, 626, 396
- Postnov, K., Oskina, L., & Torrejón, J. M. 2017, *MNRAS*, 465, L119
- Pradhan, P., Huenemoerder, D. P., Ignace, R., Nichols, J. S., & Pollock, A. M. T. 2023, *ApJ*, 954, 123
- Scargle, J. D., Norris, J., & Jackson, B. 2006, in *Studies in Astronomical Time Series Analysis*. VI
- Scargle, J. D., Norris, J. P., Jackson, B., & Chiang, J. 2013, *ApJ*, 764, 167
- Tsujimoto, M., Hayashi, T., Morihana, K., & Moritani, Y. 2023, *PASJ*, 75, 177
- Tsujimoto, M., Morihana, K., Hayashi, T., & Kitaguchi, T. 2018, *PASJ*, 70, 109
- Warner, B. 1983, in *Astrophysics and Space Science Library*, Vol. 101, *IAU Colloq. 72: Cataclysmic Variables and Related Objects*, ed. M. Livio & G. Shaviv, 155–171
- Yuasa, T., Nakazawa, K., Makishima, K., et al. 2010, *A&A*, 520, A25